

# Selenite Reduction by Mackinawite, Magnetite and Siderite: XAS Characterization of Nanosized Redox Products

ANDREAS C. SCHEINOST<sup>\*,†</sup> AND LAURENT CHARLET<sup>‡</sup>

*Institute of Radiochemistry, Forschungszentrum Dresden-Rossendorf (FZD), 01314 Dresden, Germany, and Geochemistry Group, LGIT, Université Joseph-Fourier, B.P. 53, 38041 Grenoble, France*

*Received June 27, 2007. Revised manuscript received October 30, 2007. Accepted December 10, 2007.*

Suboxic soils and sediments often contain the Fe(II)-bearing minerals mackinawite (FeS), siderite (FeCO<sub>3</sub>) or magnetite (Fe<sub>3</sub>O<sub>4</sub>), which should be able to reduce aqueous selenite, thereby forming solids of low solubility. While the reduction of selenate or selenite to Se(0) by green rust, pyrite and by Fe<sup>2+</sup> sorbed to montmorillonite is a slow (weeks), kinetically limited redox reaction as demonstrated earlier, we show here that selenite is rapidly reduced within one day by nanoparticulate mackinawite and magnetite, while only one third of selenite is reduced by micrometer-sized siderite. Depending on Fe(II)-bearing phase and pH, we observed four different reaction products, red and gray elemental Se, and two iron selenides with structures similar to Fe<sub>7</sub>Se<sub>8</sub> and FeSe. The thermodynamically most stable iron selenide, ferroselite (FeSe<sub>2</sub>), was not observed. The local structures of the reaction products suggest formation of nanoscale clusters, which may be prone to colloid-facilitated transport, and may have a higher than expected solubility.

## Introduction

The radioactive isotope <sup>79</sup>Se is a long-lived fission product (half-life 4.8 × 10<sup>5</sup> to 1.1 × 10<sup>6</sup> years *1, 2*), which may dominate the radiation dose from high-level radioactive waste for 10<sup>5</sup> years according to several national risk assessment reports (e.g., refs 3,4). Mobility and bioavailability of Se is hence a major concern for the safe enclosure of nuclear waste. Selenium solubility is largely controlled by Se oxidation state, therefore depends on redox conditions in soils, sediments, and aquifers (5, 6). The higher oxidation states +VI and +IV prevail as mobile aqueous oxyanions, while the oxidation states 0, -I, and -II prevail as solids with low solubility (7). Along redox gradients, soluble selenate (Se(VI)) or selenite (Se(IV)) species migrate toward regions of low Eh, where they precipitate as elemental Se, thereby creating an efficient sink for Se (8–10). Microorganisms play an important role in this process, since Se(VI) and Se(IV) oxyanions may act as terminal electron acceptors of anaerobic microbial respiration (11, 12). However, Se is also reduced abiotically by Fe(II)-containing solids, e.g., at the surface of the Fe(II)Fe(III) hydroxide, green rust (13, 14), or at the surface of pyrite (15).

The Fe<sup>2+</sup> hexaqua ion, which is ubiquitous in water-logged soils and aquifers, does not seem to reduce selenite. When it is adsorbed by clay minerals, however, it reduces Se in a slow reaction, which continues for several weeks (16). The Se reduction is kinetically decoupled from the rapid oxidation of Fe(II) to Fe(III), most likely by formation and storage of an hydrogen intermediate at the clay mineral surface (17).

Both biotic and abiotic reactions seem to reduce Se predominantly to elemental Se, identified as the amorphous or red allotrope by XANES spectroscopy or by the color change observed in samples with low opacity (18, 19). There is only one report on the formation of a small amount of Se(-II) on green rust, but since Se(0) prevailed this species could not be identified (13). In contrast, reduced Se forms like ferroselite, dzharkenite and Se-substituted pyrite are commonly observed in soils, sediments, and ore deposits suggesting their thermodynamic stability under a relatively wide range of geochemical conditions (20–23).

Here, we present data on the selenite reduction behavior of magnetite, mackinawite, and siderite, which are Fe(II)-containing mineral phases relevant for natural aquifer settings as well as for engineered barriers and nuclear waste containers (24–26). These minerals have been shown to reduce a range of redox sensitive metals like V, Cr, Fe, Tc, U, and Np (27–29). Special care was taken to work under strictly anoxic conditions (<1 ppmv O<sub>2</sub>) for sample preparation and spectroscopic characterization. The Se redox products were characterized by X-ray absorption spectroscopy (XAS), using the XANES (X-ray Absorption Near-Edge Structure) region to identify Se oxidation state and coordination, and the EXAFS (Extended X-ray Absorption Fine-Structure) region to elucidate the short-range structure.

## Materials and Methods

Magnetite, mackinawite and siderite samples were prepared and stored as suspensions under strictly anoxic conditions (<1 ppmv O<sub>2</sub>) in a Jacomex glovebox as described in more detail in the Supporting Information. Both magnetite and mackinawite are nanoparticulate with mean particle sizes between 2 and 10 nm. The siderite particles have a mean diameter of 3 μm.

Selenium adsorption and reduction in the presence of mackinawite, siderite, and magnetite was studied in a closed reactor in free pH drift mode. At time zero, an aliquot of a Se(IV) stock solution at pH 6.0 was introduced into the glass reactor to obtain initial solution concentrations of 0.99–9.09 mM (Table 1). After given reaction periods 10 mL of suspension were filtered through a 0.22 μm pore size membrane and analyzed for selenium concentration. The wet pastes were then transferred to XAS sample holders, shock-frozen with liquid N<sub>2</sub>, and transported in a Dewar filled with liquid N<sub>2</sub> to the synchrotron facility, where they were transferred to a closed-cycle He cryostat with He atmosphere and 15 K temperature for the XAS measurement.

XANES and EXAFS spectra were collected at the Rossendorf Beamline at ESRF (Grenoble, France) using a 13 element high-purity germanium detector (Canberra) with digital signal processing (XIA) for fluorescence detection. The monochromator energy was calibrated with a gold foil (K-edge at 11919 eV) because of its greater inertness and hence reliability in comparison to elemental Se. With this approach, we determined an edge energy of 12656 eV for trigonal Se, instead of the tabulated value of 12658 eV for zerovalent Se. Dead time correction of the fluorescence signal, energy calibration and the averaging of single scans were performed with the

\* Corresponding author phone: +33 476 88 24 62; fax: +33 476 88 25 52; e-mail: scheinost@esrf.fr

† Forschungszentrum Dresden-Rossendorf (FZD).

‡ Université Joseph-Fourier.

TABLE 1. Summary of Experimental Conditions

sample code	mineral	mineral suspension added (mL)	[Fe] <sub>T</sub> (mmol/L)	[Se] <sub>ini</sub> (mmol/L)	reaction Time	pH <sub>ini</sub>	pH <sub>end</sub>	[Fe] <sup>II</sup> <sub>s</sub> (mmol/L)	[Se] <sub>s</sub> (mmol/L)
Mack 4 h pH 4	mackinawite	15	297	0.99	4 h	4.4	7.6	2.8	<6.3 10 <sup>-5</sup>
Mack 4 h	mackinawite	15	273	9.09	4 h	6.3	nd <sup>a</sup>	nd	nd
Mack1 day	mackinawite	15	273	9.09	1 d	6.6	9.7	<0.01	<6.3 10 <sup>-5</sup>
Sid 1 day	siderite	10	198	0.99	1 d	8.0	8.3	0.04	<6.0 10 <sup>-3</sup>
Magn 1 day	magnetite	10	540	0.99	1 d	5.0	5.3	30	<6.3 10 <sup>-5</sup>

<sup>a</sup> nd, not determined.

software package SixPack. Shell fitting was done in WinXAS. Wavelet analysis was performed with the FORTRAN program HAMA, which may be downloaded at <http://www.esrf.fr/UsersAndScience/Experiments/CRG/BM20/Software/Wavelets/Wavelets> (30). The Morlet wavelet was used with the parameter  $\eta \times \sigma = 5$ , thereby optimizing the resolution in k-space at the distance of the coordination shell.

## Results and Discussion

**Reference Phases.** While XAS is the method of choice to investigate oxidation state and structure of elements in complex matrices, the versatility of structural components and hence multitude of solid phases with only slightly varying atomic distances makes their phase identification based on shell fitting often difficult (23, 31). This is also true for candidate phases of Fe(II)-driven selenite reduction, elemental Se allotropes, and iron selenides. In spite of a variety of structures, distances of the coordination sphere fall in a narrow window 2.33–2.41 Å except for achavalite (2.56) (Supporting Information Figure S1). Furthermore, second shell atoms are spread out with multiple distances separated by 0.1–0.2 Å, which is at the limit of EXAFS resolution and causes signal loss by destructive interferences. Hence, a careful analysis of reference phases is mandatory before attempting to interpret spectra of unknown phases.

Figure 1a shows the XANES spectra of three phases with formal oxidation states 0 (trigonal Se), -I (ferroselite), and -II (tetragonal FeSe). With each additional valence electron, the edge is shifted by about 1 eV to lower energy due to a decrease of the effective nuclear charge. While this small shift of edge energy may be masked by differences of the coordination geometry via multiple scattering effects, the identification of Se oxidation states is further supported by the relative intensity of the white line. This peak, formally assigned to a 1s → 4p transition, is significantly reduced in height for each additional valence electron (see arrows) due to an increased population of the valence 4p levels (32). Both the edge shift and structure of the 1s → 4p transition of ferroselite are in line with an oxidation state of -I like that of S in pyrite (33). The difference between oxidation state -I and -II could be further confirmed by self-consistent XANES simulation with FEFF 8.2 (34) using the following parameters (Hedin-Lundquist; EXCHANGE 0; SCF 6.0; XANES 6.0; FMS 8.0, 0; LDOS -30, 20, 0.1) and the crystallographic structures of ferroselite, dzharkenite, tetragonal FeSe, and hexagonal FeSe (Figure S2 in the Supporting Information).

The discrimination of elemental Se from Fe(II) selenides is also possible by identifying the neighbors in the coordination sphere, which are Se in elemental Se, and prevalently Fe in Fe selenides (Supporting Information Figure S1). However, EXAFS shell fitting was not sufficient to this purpose since fits with either Se or Fe backscatterers achieved both low fit errors and reasonable values of coordination numbers, distances, and Debye-Waller factors, making the discrimination of Se and Fe impossible. Therefore, we employed wavelet analysis which has a superior resolution for the amplitude envelop in k-space and, hence, for the

elemental nature of backscattering atoms (30). Figure 2 shows the clear separation in k-space of Fe (6.0–6.5 Å<sup>-1</sup>) and Se backscatterers (7.0–7.4 Å<sup>-1</sup>) for tetragonal FeSe and trigonal Se, respectively. Note that the center of ferroselite (not shown) was shifted to the left (≈5.5 Å<sup>-1</sup>).

Based on the a priori classification of solid phases by XANES and wavelet analysis, distances and coordination numbers of the references could be derived by shell fitting. For trigonal Se, distances up to 5 Å are identical to those derived by XRD (35) with the exception of the first shell, which is 0.02 Å longer (Table 2). The fit of tetragonal FeSe shows deviations of up to 0.05 Å or 1.3% from the crystallographic values. These deviations are both in the positive and the negative directions, and do not seem to correlate with changes of the unit-cell dimension. In fact, the XRD pattern of this sample is identical in peak positions and very close in relative peak intensities to the corresponding pattern of Haegg and Kindstroem (36). The deviations could, hence, indicate an unresolved problem of this early work. For orthorhombic FeSe<sub>2</sub>, the mineral ferroselite, the first coordination shell could be reliably fitted, achieving distances comparable to the crystallographic data (37). Three-legged and four-legged multiple scattering (MS) paths are responsible for the Fourier transform peak at 4.4 Å (uncorrected for phase shift). The fitted MS path length of twice the distance of the Fe coordination shell confirmed the reliability of the fitting approach. The peaks between the coordination shell and the MS peaks, however, are due to a large variety of distances which exceed the shell resolution of EXAFS (≈0.12 Å in the given k-range 3–16 Å<sup>-1</sup>) precluding a reliable fit of these distances. Attempts were made to combine similar paths, Table 2 showing the data of the simplest model with a reasonable fit of the spectrum.

**Selenite Reduction by Mackinawite.** According to their white line peaks, the three mackinawite samples can be divided into two groups, sample “Mack 4 h pH 4” with a Se oxidation state of -II, and samples “Mack 4 h” and “Mack 1 d” with Se(0) (Figure 1c). This assignment is corroborated by the wavelet analysis, which shows that Se is coordinated to Fe atoms in the former, and coordinated to Se atoms in the two latter samples (Figure 2).

While the three samples appear to be almost identical based on their EXAFS Fourier transform spectra, the unfiltered EXAFS spectra show significant differences in phase shift and amplitude at low k (see arrow in Figure 1d). For the sample at pH 4.3, these features are similar to those of tetragonal FeSe, while at higher pH the features are similar to those of nanoparticulate red Se. Due to an obvious lack of structural features beyond 2.5 Å except for small peaks at about 3.3 and 4.2 Å (uncorrected for phase shift), however, the spectra of the sample at pH 4.3 shows large differences from those of the tetragonal FeSe reference. In contrast, spectral features of the samples at higher pH are similar to those of nanoparticulate red Se.

Table 2 gives the structural data as derived by EXAFS shell fitting. For the 4-h and 1-d samples, the first-shell distance of 2.34 Å is significantly smaller (error < ± 0.01 Å) than that

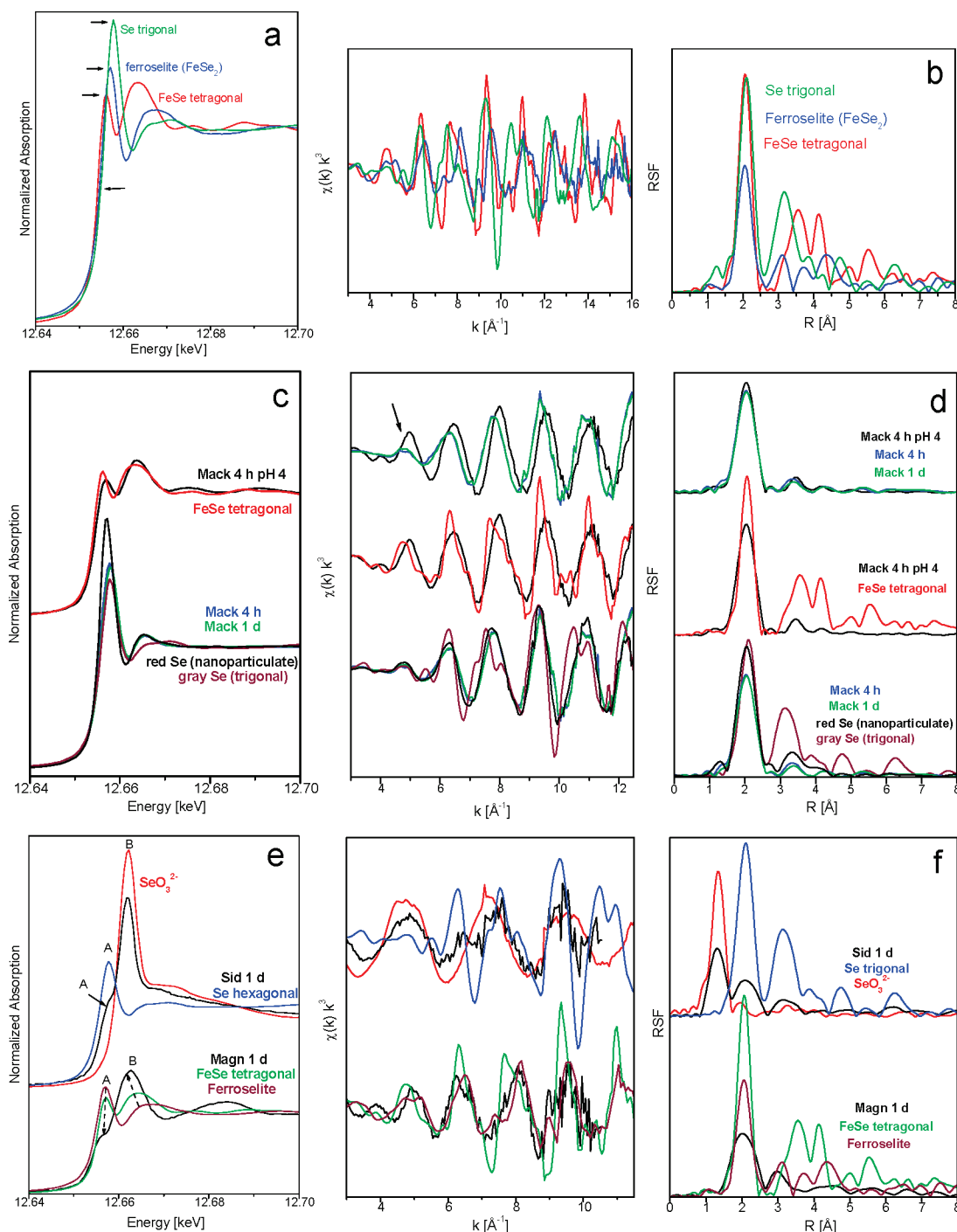


**FIGURE 1.** Se K-edge XANES (a, c, e) and EXAFS spectra (b, d, f) of redox samples and of selected references. (a, b) Trigonal Se, ferroselite ( $\text{FeSe}_2$ ) and tetragonal FeSe. (c, d) Selenite reduced by nanoparticulate mackinawite ( $\text{FeS}$ ). (e, f) Selenite reduced by siderite ( $\text{FeCO}_3$ ) and by nanoparticulate magnetite ( $\text{Fe}_3\text{O}_4$ ).

of trigonal Se (2.39 Å), and is closer to the corresponding distance of the red Se reference. A second shell at 3.38–3.39 Å occurring in both gray and red Se references is completely missing, while the third shell at 3.67–3.69 is again in line with red Se and with the XRD-structure of  $\alpha$ -monoclinic Se (38). The fitted EXAFS spectra of one of the samples and of the red Se reference are given in Supporting Information Figure S3. The smaller coordination numbers of the mackinawite samples for shells beyond the coordination sphere, in comparison to those of the 5 nm red Se reference, suggest that the size of structurally coherent regions is below one nanometer in the reacted samples.

For the 4 h sample at the lower pH 4.4, the fitted distances of 2.38 Å (Fe), 3.59 Å (Se) and 4.42 Å (Fe) do not match those of tetragonal FeSe with 2.37 Å (Fe), 3.76 Å (Se), 3.91 Å (Se), and 4.45 Å (Fe). While the two longer distances are close to those of hexagonal FeSe (achavalite), 3.62 Å (Se) and 4.43 Å (Fe), the distance of the first shell is too short in comparison to that of achavalite (2.56 Å) (39). Again, the lack of observable structural features above 4.5 Å and the small coordination numbers (1.2 instead of 12 for the second shell) point toward a small cluster size in the order of 1 nm.

**Selenite Reduction by Siderite.** After 1 day reaction time, the XANES spectrum of the siderite sample is dominated by



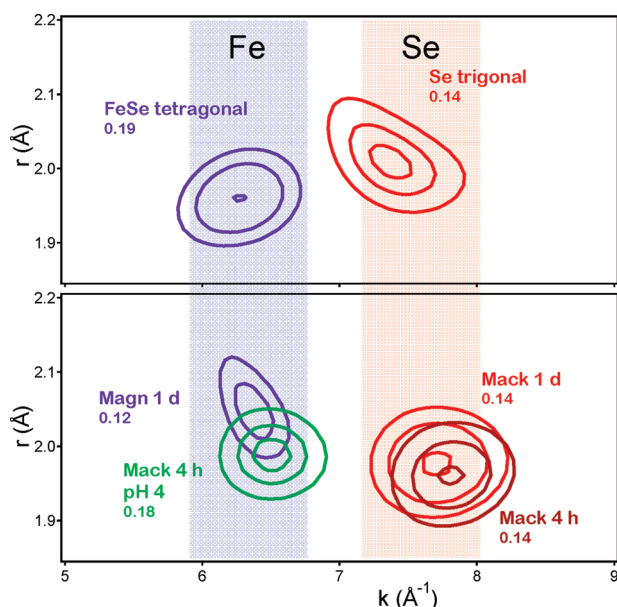


**FIGURE 2.** Wavelet analysis of Se-K EXAFS spectra of references (top) and samples (bottom). The  $k$ -regions, where 1st shell maxima of Fe and Se backscatters are expected are marked in blue and red, respectively. Values for peak heights are given below the sample labels.

the strong white line of Se(IV) (labeled “B” in Figure 1e), and the EXAFS Fourier transform shows the presence of an oxygen coordination shell at about 1.4 Å (uncorrected for phase shift, Figure 1f), hence unreduced selenite is still present after one day. A small shoulder in the edge, however, with an inflection point at 12656.0 eV (“A” in Figure 1e), and the EXAFS fit result with 0.6 Se atoms at 2.38 Å suggests partial reduction to elemental Se (Table 2). To quantify the relative amount of both species, linear combination fit of XANES and EXAFS using either red or trigonal Se, and aqueous selenite as input variables was performed. Trigonal Se produced better fit results, with a consistent distribution of  $2/3$  selenite and  $1/3$  Se in the siderite sample.

**Selenite Reduction by Magnetite.** For the magnetite sample, the XANES edge position indicates oxidation state -II (Figure 1e). The narrow white line peak typical for FeSe phases is not present, however, and appears only as a shoulder in the edge (labeled “A” in Figure 1e). The first pronounced peak, B, is almost 20 eV behind the edge and at almost the same position as the white line of Se(IV). At first glance, the spectrum looks similar to that of siderite, i.e. like a mixture of reduced and nonreduced Se species. On closer inspection, however, this peak is much broader than that of  $\text{SeO}_3^{2-}$ , and the EXAFS Fourier transform does not reveal any traces of an oxygen shell (Figure 1f), indicating a complete reduction of selenite. Furthermore, the wavelet analysis indicates the prevalence of Fe in the coordination sphere (Figure 2). The first pronounced peak B of XANES is, therefore, not the  $1s \rightarrow 4p$  transition (which occurs as small shoulder, A), but is caused by multiple scattering in the coordination sphere. The lower energy of B in comparison to the references is most likely caused by a shorter Se–Fe distance (note the shift from ferroselite to tetragonal FeSe to Magn 1 d), as confirmed by the shell fit (2.31 Å). The low intensity of the electron transition band A suggests a population of the valence 4p level below that of the tetragonal FeSe sample. Since oxidation states below -II are not reasonable to assume, this effect may be due to a change of the bonding character, e.g. an increase of the covalency of the Se–Fe bond due to the shorter distance. In fact, theoretical XANES spectra (Supporting Information Figure S2a) calcu-

lated by FEFF and based on the crystallographic structures predicted a substantially lower white line for tetragonal FeSe in comparison to achavalite, in line with this explanation. Therefore, we maintain that the formed species is an iron selenide with Se oxidation state of -II.

EXAFS shell fitting was applied to further elucidate the structure of this species. The broad first-shell peak required a fit with two Fe distances at 2.31 and 2.42 Å (Table 2). A second shell was fit with Se at 3.44 Å. These distances do not match those of tetragonal or hexagonal FeSe. They would agree with the structure of dzharkenite, but from XANES we concluded that Se oxidation state is -II rather than -I. The closest match of Se(-II) structures is trigonal  $\text{Fe}_3\text{Se}_8$ , which has one Fe atom at 2.33 Å, followed by four Fe atoms at distances from 2.47 to 2.54 Å and 12 Se atoms at 3.54–3.62 Å (40). The small coordination number for the second shell, 5.7 Se as compared to the expected 12, suggests formation of nanoscale clusters with an average diameter of 5 Å, which may be structurally different from macrocrystalline solids.

**Reaction Processes and Environmental Relevance.** Depending on pH and the Fe(II)-mineral present, four different solid phases precipitated after selenite reduction: two phases with zerovalent Se, red Se, and trigonal Se, and two phases with oxidation state -II, one structure similar to tetragonal FeSe, and one similar to  $\text{Fe}_3\text{Se}_8$ . In contrast to previous investigations, which observed elemental Se in abiotic, heterogeneous redox reactions with green rust, pyrite, and  $\text{Fe}^{2+}$ -sorbed clay (13–16), this is the first observation and identification of Se(-II) solids.

The comparison of redox reaction products in presence of mackinawite at two different pH values, FeSe at pH 4.4, and elemental Se at pH 6.3, suggest an influence of mackinawite solubility as source of Fe for the subsequent FeSe precipitation. Mackinawite solubility increases by about 4 orders of magnitude when decreasing the pH from 6.6 to 4.4 ( $K_s^{\text{app}} = \{\text{Fe}^{2+}\}\{\text{H}_2\text{S}(\text{aq})\}\{\text{H}^+\}^{-2} = 10^{+4.87}$ ) (41, 42).

Because only a small fraction of total Fe is converted during the redox reaction, the final Fe solid cannot be determined by Fe-K XAS or Mössbauer spectroscopy. Nevertheless, there are likely reaction pathways based on the assumption of heterogeneous surface reactions (43) which allow us to establish tentative reaction equations using the established Se end products. Assuming a surficial oxidation of mackinawite, the reaction at pH 4.4 is:  $6\text{Fe}^{\text{II}} + \text{HSeO}_3^- + \text{FeS} + 6\text{H}^+ \rightarrow 6\text{Fe}^{\text{III}} + \text{FeSe} + \text{HS}^- + 3\text{H}_2\text{O}$  and at pH 6.3:  $4\text{Fe}^{\text{II}} + \text{HSeO}_3^- + 5\text{H}^+ \rightarrow 4\text{Fe}^{\text{III}} + \text{Se}(\text{s}) + 3\text{H}_2\text{O}$ . Note the large pH drift to higher values suggesting a considerable consumption of protons during the reaction (Table 1). For siderite, the most likely iron phase forming at pH 8 is magnetite; hence  $6\text{Fe}^{\text{II}}\text{CO}_3(\text{s}) + \text{HSeO}_3^- + 5\text{H}_2\text{O} \rightarrow 2\text{Fe}^{\text{II}}\text{Fe}^{\text{III}}_2\text{Se}_8(\text{s}) + 8\text{OH}^-$ . For magnetite, the most likely iron redox phase is maghemite; hence,  $53\text{Fe}^{\text{II}}\text{Fe}^{\text{III}}_2\text{O}_4(\text{s}) + 8\text{HSeO}_3^- \rightarrow 76\text{Fe}_2\text{O}_3(\text{s}) + \text{Fe}^{\text{II}}\text{Fe}^{\text{III}}_8\text{Se}_8(\text{s}) + 8\text{OH}^-$ . Considering previous observations that Se redox reaction are kinetically controlled and proceed in time scales of weeks (5, 13, 16), the complete reduction of Se within several hours in the mackinawite and magnetite systems is rather surprising. However, one has to consider that both phases consist of nanoparticles with  $\leq 10$  nm in diameter with a much higher reactivity than crystals in the micrometer-range (44). This is confirmed by the siderite system with a mean particle diameter of 3  $\mu\text{m}$ , where only  $1/3$  of selenite was reduced within one day. Since siderite has a much higher solubility than mackinawite or magnetite under the given experimental conditions, this is an indication that surface area is the limiting parameter, confirming that the observed Se reduction is a heterogeneous reaction at the mineral surface.

Due to the ubiquity of nanoparticulate mackinawite (synonymous to acid volatile sulfide (42)), magnetite and

**TABLE 2. Se-K XANES Edge Energies and EXAFS Fit Results of Redox Samples and References**

sample (mineral, space group)	$E_0$ [eV]	coordination shell			further shells			$\Delta E_0$ [eV]	$\chi^2_{\text{res}}$ %	coordination XRD		further shells XRD	
		CN <sup>a</sup>	$R^b$ (Å)	$\sigma^2$ (Å <sup>2</sup> )	CN	$R$ (Å)	$\sigma^2$ (Å <sup>2</sup> )			CN	$R$ (Å)	CN	$R$ (Å)
gray Se (trigonal P 31 2 1)	12656.1	2 Se	2.39	0.0028	4 Se	3.38	0.0066	8.0	5.1	2 Se	2.37	4 Se	3.38
					2 Se	3.74	0.0048					2 Se	3.74
					6 Se	4.30	0.0070					6 Se	4.30
					4 Se	4.45	0.0052					4 Se	4.45
					4 Se	4.94	0.0059					4 Se	4.94
red Se nanopart. (P1 21/n1)	12655.9	2.1 Se	2.36	0.0027	1.0 Se	3.39	0.0058	8.0	4.4	2 Se	2.33	9 Se	3.66–3.99
					1.4 Se	3.69	0.0066						
					1.2 Se	4.36	0.0062						
orthorhombic FeSe <sub>2</sub> (ferroselite, P n n m)	12655.3	3 Fe	2.38	0.0035	2.7 Se	3.35	0.0061	12.4	6.8	3 Fe	2.37	5 Se	3.14–3.30
		1 Se	2.56	0.0047	0.7 Se	3.70	0.0039			1 Se	2.53	6 Se	3.42–3.58
					1.6 Fe	3.93	0.0014					3 Fe	3.78–3.93
					1.6 Se	4.33	0.0042					3 Fe	4.30–4.34
tetragonal FeSe (P 4/n m m)	12654.4	4 Fe	2.38	0.0019	8 Se	3.71	0.0070	4.7	7.3	4 Fe	2.37	8 Se	3.76–3.77
					4 Se	3.95	0.0030					4 Se	3.91
					12 Fe	4.44	0.0047					12 Fe	4.45–4.50
Mack 4 h pH 4	12654.7	4.1 Fe	2.38	0.0024	1.2 Se	3.59	0.0027	7.4	7.3				
					2.0 Se	4.42	0.007						
Mack 4 h	12655.8	2.1 Se	2.34	0.0025	0.7 Se	3.67	0.0038	6.5	1.7				
Mack 1 d	12655.8	2.1 Se	2.34	0.0027	0.6 Se	3.69	0.0036	7.2	4.1				
					0.3 Se	4.71	0.0012						
Sid 1 d	12656.0	1.3 O	1.68	0.0010				15.1	2.6				
	12660.4	0.6 Se	2.38	0.0020									
Magn 1 d	12654.3	1.0 Fe	2.31	0.0018	5.7 Se	3.44	0.0100	7.4	8.8				
		2.8 Fe	2.42	0.0033									

<sup>a</sup> CN: coordination number, error  $\pm 25\%$ . <sup>b</sup> R: Radial distance, error  $\pm 0.01$  Å. <sup>c</sup>  $\sigma^2$ : Debye–Waller factor, error  $\pm 0.0005$  Å<sup>2</sup>.

microparticulate siderite in oxygen-poor subsurface environments like sediments, aquifers, or nuclear waste disposal sites, selenite may be rapidly reduced to elemental Se or iron selenites with low solubility in such environments, creating an efficient sink for Se. In fact in all cases, where selenite was completely reduced, the Se concentration dropped below  $6.3 \times 10^{-5}$  mmol/L (the lower detection limit of ICP-MS, Table 1), whereas it was reduced by only two orders of magnitude in the presence of siderite, where only part of selenite was reduced. However, one has to consider that reaction rates in natural systems may be much slower due to competing processes like sorption to clay minerals and humic substances (15). Furthermore, the solubility of nano-sized clusters may be several orders of magnitude higher than those of larger particles (45). Finally, due to their colloidal properties such clusters may detach from the surface and form stable suspensions under specific physicochemical groundwater conditions (mainly low ionic strength and pH different from the point of zero charge) (46). In this case, elemental Se and iron selenides may be transported within aquifers across long distances, causing an unwanted distribution and in case of a reoxygenation of the aquifer waters, a drastic increase in bioavailability and toxicity. Further experiments are required to study these effects, including longer reaction periods relevant for natural systems, a systematic variation of pH, initial Se concentration and surface area,  $\gamma$ -spectroscopy to determine the solubilities too low for conventional techniques like ICP-MS, additional (spectroscopic) approaches to quantify the amount of oxidized Fe and S and its chemical speciation, and finally column or lysimeter experiments to study the Se breakthrough behavior.

## Acknowledgments

This work was supported by the EU through RECOSEY and ACTINET European Network of Excellence. We thank Antoine Géhin for the synthesis of mackinawite, siderite and magnetite, Harald Funke for performing the wavelet analysis, Daniel Strawn (University of Idaho) for providing the XAS spectrum of synthetic ferroselite, and Serguej Nikitenko (Université de Bordeaux, France) for providing the nanoparticulate red Se.

## Note Added after ASAP Publication

This paper published ASAP February 13, 2008 with an equation error in the third paragraph of the Reaction Processes and Environmental Relevance section; a revised version published ASAP February 14, 2008.

## Supporting Information Available

More detailed information on methods, and figures with structural models of elemental Se allotropes and Fe selenides, theoretical XANES and EXAFS spectra of references and examples of EXAFS shell fits. This material is available free of charge via the Internet at <http://pubs.acs.org>.

## Literature Cited

- Magill, J.; Pfennig, G.; Galy, J. Chart of the Nuclides; 7th ed.; European Commission - DG Joint Research Centre—Institute of Transuranium Elements: Karlsruhe, 2006.
- Jiang, S.; Guo, J.; Jiang, S.; Li, C.; Cui, A.; He, M.; Wu, S.; Li, S. Determination of the half-life of <sup>79</sup>Se with the accelerator mass spectrometry technique. *Nucl. Instrum. Methods Phys. Res., Sect. B* **1997**, *123*, 405–409.

- (3) Chen, F.; Burns, P. C.; Ewing, R. C. 79Se: geochemical and crystallo-chemical retardation mechanisms. *J. Nucl. Mater.* **1999**, 275, 81–94.
- (4) Becker, D.-A.; Buhmann, D.; Storck, R.; Alonso, J.; Cormenzana, J.-L.; Hugi, M.; Gemert, F. v.; O'Sullivan, P.; Laciok, A.; Marivoet, J.; Sillen, X.; Nordman, H.; Vieno, T.; Niemeyer, M. Testing of Safety and Performance Indicators (SPIN).; European Commission, 2002.
- (5) Masscheleyn, P. H.; Delaune, R. D.; William, H. P. Transformations of selenium as affected by sediment oxidation-reduction potential and pH. *Environ. Sci. Technol.* **1990**, 24, 91–96.
- (6) Séby, F.; Potin-Gautier, M.; Giffaut, E.; Donard, O. F. X. Assessing the speciation and the biogeochemical processes affecting the mobility of radioactive wastes to the biosphere. *Analysis* **1998**, 26, 193–198.
- (7) Elrashidi, M. A.; Adriano, D. C.; Workman, S. M.; Lindsay, W. L. Chemical equilibria of selenium in soils: a theoretical development. *Soil Sci.* **1987**, 144, 141–152.
- (8) Tokunaga, T. K.; Brown, G. E.; Pickering, I. J.; Sutton, S. R.; Bait, S. Selenium redox reactions and transport between ponded waters and sediments. *Environ. Sci. Technol.* **1997**, 31, 1419–1425.
- (9) Tokunaga, T. K.; Sutton, S. R.; Bajt, S.; Nuessle, P.; Shear-McCarthy, G. Selenium diffusion and reduction at the water-sediment boundary: micro-XANES spectroscopy of reactive transport. *Environ. Sci. Technol.* **1998**, 32, 1092–1098.
- (10) Zhang, Y. Q.; Moore, J. N. Interaction of selenate with a wetland sediment. *Appl. Geochem.* **1997**, 12, 685–691.
- (11) Oremland, R. S.; Hollibaugh, J. T.; Maest, A. S.; Presser, T. S.; Miller, L. G.; Culbertson, C. W. Selenate reduction to elemental selenium by anaerobic bacteria in sediments and culture: Biogeochemical significance of a novel, sulfate-independent respiration. *Appl. Environ. Microbiol.* **1989**, 55, 2333–2343.
- (12) Stolz, J. F.; Oremland, R. S. Bacterial respiration of arsenic and selenium. *FEMS Microbiol. Rev.* **1999**, 23, 615–627.
- (13) Myneni, S. C. B.; Tokunaga, T. K.; Brown, G. E. Abiotic selenium redox transformations in the presence of Fe(II,III) oxides. *Science* **1997**, 278, 1106–1109.
- (14) Scheidegger, A. M.; Grolimund, D.; Cui, D.; Devoy, J.; Spahiu, K.; Wersin, P.; Bonhoure, I.; Janousch, M. Reduction of selenite on iron surfaces: A micro-spectroscopic study. *J. Phys. IV* **2003**, 104, 417–420.
- (15) Bruggeman, C.; Maes, A.; Vancluysen, J.; Vandemussele, P. Selenite reduction in Boom clay: Effect of FeS<sub>2</sub>, clay minerals and dissolved organic matter. *Environ. Pollut.* **2005**, 137, 209–221.
- (16) Charlet, L.; Scheinost, A. C.; Tournassat, C.; Greneche, J. M.; Géhin, A.; Fernández-Martínez, A.; Coudert, S.; Tisserand, D.; Brendle, J. Electron transfer at the mineral/water interface: Selenium reduction by ferrous iron sorbed on clay. *Geochim. Cosmochim. Acta* **2007**, in print.
- (17) Géhin, A.; Greneche, J.-M.; Tournassat, C.; Brendle, J.; Rancourt, D. G.; Charlet, L. Reversible surface-sorption-induced electron-transfer oxidation of Fe(II) at reactive sites on a synthetic clay mineral. *Geochim. Cosmochim. Acta* **2007**, 71, 863–876.
- (18) Garbisu, C.; Ishii, T.; Leighton, T.; Buchanan, B. B. Bacterial reduction of selenite to elemental selenium. *Chem. Geol.* **1996**, 132, 199–204.
- (19) Buchanan, B. B.; Bucher, J. J.; Carlson, D. E.; Edelstein, N. M.; Hudson, E. A.; Kaltsoyannis, N.; Leighton, T.; Lukens, W.; Nitsche, H.; Reich, T.; Roberts, K.; Shuh, D. K.; Torretto, P.; Woicik, J.; Yang, W.-S.; Yee, A.; Yee, B. C. AXANES and EXAFS investigation of the speciation of selenite following bacterial metabolism. *Inorg. Chem.* **1995**, 34, 1617–1619.
- (20) Howard, J. H. Geochemistry of selenium-Formation of ferroselite and selenium behavior in vicinity of oxidizing sulfide and uranium deposits. *Geochim. Cosmochim. Acta* **1977**, 41, 1665–1678.
- (21) Xiong, Y. L. Predicted equilibrium constants for solid and aqueous selenium species to 300 degrees C: applications to selenium-rich mineral deposits. *Ore Geol. Rev.* **2003**, 23, 259–276.
- (22) Belzile, N.; Chen, Y. W.; Xu, R. R. Early diagenetic behaviour of selenium in freshwater sediments. *Appl. Geochem.* **2000**, 15, 1439–1454.
- (23) Ryser, A. L.; Strawn, D. G.; Marcus, M. A.; Johnson-Maynard, J. L.; Gunter, M. E.; Möller, G. Micro-spectroscopic investigation of selenium-bearing minerals from the Western US Phosphate Resource Area. *Geochem. Trans.* **2005**, 6, 1–11.
- (24) Spadini, L.; Bott, M.; Wehrli, B.; Manceau, A. Analysis of the major Fe bearing phases in recent lake sediments by EXAFS spectroscopy. *Aquatic Geochemistry* **2003**, 9, 1–17.
- (25) Phillips, D. H.; Watson, D. B.; Roh, Y.; Gu, B. Mineralogical characteristics and transformations during long-term operation of a zerovalent iron reactive barrier. *J. Environ. Qual.* **2003**, 32, 2033–2045.
- (26) Smailos, E.; Schwarzkopf, W.; Kienzler, B.; Köster, R. Corrosion of carbon-steel container for heat-generating nuclear waste in brine environment relevant for a rock-salt repository. *Mater. Res. Soc. Symp. Proc.* **1992**, 257, 399–406.
- (27) Livens, F. R.; Jones, M. J.; Hynes, A. J.; Charnock, J. M.; Mosselmans, J. F. W.; Hennig, C.; Steele, H.; Collison, D.; Vaughan, D. J.; Patrick, R. A. D.; Reed, W. A.; Moyes, L. N. X-ray absorption spectroscopy studies of reactions of technetium, uranium and neptunium with mackinawite. *J. Environ. Radioact.* **2004**, 74, 211–219.
- (28) White, A. F.; Peterson, M. L. Reduction of aqueous transition metal species on the surface of Fe(II)-containing oxides. *Geochim. Cosmochim. Acta* **1996**, 60, 3799–3814.
- (29) Erdem, M.; Gur, F.; Tumen, F. Cr(VI) reduction in aqueous solutions by siderite. *J. Hazard. Mater.* **2004**, 113, 219–224.
- (30) Funke, H.; Scheinost, A. C.; Chukalina, M. Wavelet analysis of extended X-ray absorption fine structure data. *Phys. Rev.* **2005**, B 71, 094110.
- (31) Scheinost, A. C.; Rossberg, A.; Vantelon, D.; Xifra, I.; Kretzschmar, R.; Funke, H.; Johnson, C. A. Quantitative antimony speciation in shooting-range soils by EXAFS spectroscopy. *Geochim. Cosmochim. Acta* **2006**, 70, 3299–3312.
- (32) Pickering, I. J.; Brown, G. E.; Tokunaga, T. K. Quantitative speciation of selenium in soils using x-ray absorption spectroscopy. *Environ. Sci. Technol.* **1995**, 29, 2456–2459.
- (33) Vairavamurthy, A.; Zhou, W. Q.; Eglinton, T.; Manowitz, B. Sulfonates—A novel class of organic sulfur-compounds in marine sediments. *Geochim. Cosmochim. Acta* **1994**, 58, 4681–4687.
- (34) Ankudinov, A. L.; Rehr, J. J. Relativistic spin-dependent X-ray absorption theory. *Phys. Rev. B* **1997**, 56.
- (35) Cherin, P.; Unger, P. The crystal structure of trigonal selenium. *Acta Crystallogr.* **1966**, 21, 46.
- (36) Haegg, G.; Kindstroem, A. L. Röntgenuntersuchungen am System Eisen—Selen. *Z. Phys. Chem., B* **1933**, 22, 453–464.
- (37) Kjekshus, A.; Rakke, T.; Andresen, A. F. Compounds with the marcasite type crystal structure. IX. Structural data for Fe As<sub>2</sub>, Fe Se<sub>2</sub>, Ni As<sub>2</sub>, Ni Sb<sub>2</sub>, and Cu Se<sub>2</sub>. *Acta Chem. Scand.* **1974**, 28, 996–1000.
- (38) Cherin, P.; Unger, P. Refinement of the crystal structure of alpha-monoclinic Se. *Acta Crystallogr., B* **1972**, 28, 313–317.
- (39) Terzieff, P.; Schicketanz, H.; Komarek, K. The magnetic and thermoelectric properties of Ni As-type Fe<sub>89</sub>Se. *Monatsh. Chem.* **1982**, 113, 519–527.
- (40) Andresen, A. F.; Leciejewicz, J. A neutron diffraction study of Fe<sub>7</sub>Se<sub>8</sub>. *J. Phys. IV* **1964**, 25, 574–578.
- (41) Wolthers, M.; Charlet, L.; Van der Linde, P. R.; Rickard, D.; Van der Weijden, C. H. Surface chemistry of disordered mackinawite (FeS). *Geochim. Cosmochim. Acta* **2005**, 69, 3469–3481.
- (42) Rickard, D. The solubility of FeS. *Geochim. Cosmochim. Acta* **2006**, 70, 5779–5789.
- (43) Nakata, K.; Nagasaki, S.; Tanaka, S.; Sakamoto, Y.; Tanaka, T.; Ogawa, H. Reduction rate of neptunium(V) in heterogeneous solution with magnetite. *Radiochim. Acta* **2004**, 92, 145–149.
- (44) Luther, G. W.; Rickard, D. T. Metal sulfide cluster complexes and their biogeochemical importance in the environment. *J. Nanopart. Res.* **2005**, 7, 389–407.
- (45) Hochella, M. F. Nanoscience and technology: the next revolution in the Earth sciences. *Earth Planet. Sci. Lett.* **2002**, 203, 593–605.
- (46) Kretzschmar, R.; Borkovec, M.; Grolimund, D.; Elimelech, M. Mobile subsurface colloids and their role in contaminant transport. *Adv. Agron.* **1999**, 66, 121–194.

ES071573F